



HAL
open science

Quantum dynamics simulations of the thermal and light-induced high-spin to low-spin relaxation in $\text{Fe}(\text{bpy})_3$ and $\text{Fe}(\text{mtz})_6$

Marc Alías-Rodríguez, Miquel Huix-Rotllant, Coen de Graaf

► **To cite this version:**

Marc Alías-Rodríguez, Miquel Huix-Rotllant, Coen de Graaf. Quantum dynamics simulations of the thermal and light-induced high-spin to low-spin relaxation in $\text{Fe}(\text{bpy})_3$ and $\text{Fe}(\text{mtz})_6$. *Faraday Discussions*, 2022, 10.1039/D2FD00027J . hal-03613227

HAL Id: hal-03613227

<https://hal.science/hal-03613227>

Submitted on 18 Mar 2022

HAL is a multi-disciplinary open access archive for the deposit and dissemination of scientific research documents, whether they are published or not. The documents may come from teaching and research institutions in France or abroad, or from public or private research centers.

L'archive ouverte pluridisciplinaire **HAL**, est destinée au dépôt et à la diffusion de documents scientifiques de niveau recherche, publiés ou non, émanant des établissements d'enseignement et de recherche français ou étrangers, des laboratoires publics ou privés.

Cite this: DOI: 00.0000/xxxxxxxxxx

Quantum dynamics simulations of the thermal and light-induced high-spin to low-spin relaxation in $\text{Fe}(\text{bpy})_3$ and $\text{Fe}(\text{mtz})_6$ [†]

Marc Alías-Rodríguez,^{*a,b} Miquel Huix-Rotllant^b and Coen de Graaf^{a,c}

Received Date

Accepted Date

DOI: 00.0000/xxxxxxxxxx

First row transition metal complexes with d^4 to d^7 electronic configuration exhibit spin-crossover (SCO), which can be induced by external stimulus such as temperature, pressure, light. The low-spin to high-spin transition has been largely studied, but very little is known about the reverse process. Here, we present a theoretical study of thermal and light-induced high-to-low spin crossover in prototypical Fe(II) complexes. The lifetime of the high-spin state in the thermal process is determined using Fermi's golden rule. With this methodology, we have accurately computed the transfer rate of the HS state thermal relaxation at several time scales (from sub-nanosecond to a few seconds) in two different iron complexes. The use of quasi-degenerate perturbation theory (QDPT2) in the analysis of the LS-HS spin-orbit coupling have allowed to identify 3T_1 as the main intermediate state coupling LS and HS states. The light-induced process has been studied using wavepacket quantum dynamics along the main vibrational coordinates (one symmetric and two asymmetric Fe-N stretchings). The study suggests that after the initial excitation from ${}^5T_{2g}$ to 5E_g state, the population is transferred back to a vibrationally hot ${}^5T_{2g}$ from which a small amount of population is transferred to the ${}^1A_{1g}$ via the intermediate ${}^3T_{1g}$. Most of the population remains trapped in the HS state at the time scale of the simulation.

Spin-crossover (SCO) is a molecular phenomena wherein the spin state of the system changes because of an external stimulus such as pressure, temperature, light irradiation or the influence of a magnetic field. This process commonly takes place from the diamagnetic thermally stable low-spin state to the paramagnetic

meta-stable high-spin state. Despite SCO can be observed in some molecules,^{1,2} the phenomena is typically appreciated in d^4 to d^7 first row transition metal complexes.³⁻⁵

Among the different transition metal complexes exhibiting spin-crossover, Fe(II) complexes have probably been the most widely studied ones. Fe(II) has a d^6 valence configuration and is usually presenting a (quasi-)octahedral coordination.⁶⁻⁹ In ferrous complexes, the magnetization varies between the diamagnetic singlet electronic state ($S=0$) and the paramagnetic quintet electronic state ($S=2$).

The magnetic bistability gives to these complexes a wide range of possible applications such as thermochromic paints, molecular switches or nanophotonic devices to name a few.¹⁰ For technological uses, low and high spin states must show a reasonable lifetime in the working temperatures, ideally room temperature. The lifetime of meta-stable high-spin states strongly depends on their adiabatic energies which makes it vary from a few picoseconds to several seconds or even days.

Hauser et al. described the thermal relaxation of the high-spin state as a tunneling process, which does not need to overcome the classical barrier.¹¹ They approximated the quantum mechanical expression for the rate constant in a tunneling process, assuming that the LS-HS spin-orbit coupling is a fixed value of 150 cm^{-1} , the vibrational frequency along the Fe-N symmetric stretching is for both the HS and LS states 250 cm^{-1} and these states are only displaced along this mode at a constant distance $\Delta r_{HL} \approx 0.2\text{ \AA}$. The so-obtained analytical expression to determine the rate of the high-spin to low-spin transition depends only on the adiabatic energy difference between these states, and is known as the energy gap rule. This approach was validated for isotropic complexes, for which the reaction coordinate is mainly a totally symmetric Fe-N breathing mode such as $[\text{Fe}(\text{bpy})_3]^{2+}$.

The light-driven mechanism for the formation of the HS state in SCO complexes, (commonly known as light-induced excited spin state trapping, LIESST) has been largely studied in Fe(II) complexes using $[\text{Fe}(\text{bpy})_3]^{2+}$ as prototype complex. Auböck et

^aDepartament de Química Física i Inorgànica, Universitat Rovira i Virgili, Marcel·lí Domingo 143007 Tarragona, Catalunya, Spain.

^bAix-Marseille Univ, CNRS, ICR, Marseille, France. E-mail: marc.alias-rodriguez@univ-amu.fr

^cICREA, Passeig Lluís Companys 23, Barcelona, Spain

[†] Electronic Supplementary Information (ESI) available: [details of any supplementary information available should be included here]. See DOI: 00.0000/00000000.

al. determined a direct transfer from the metal to ligand charge transfer ($^1,^3\text{MLCT}$) band to the ^5T state in the sub-50-fs time scale through ultrafast pump-probe spectroscopy.¹² Zhang et al. based on X-ray emission spectroscopy concluded that the population of the ^5T state was in two sequential steps, $^1,^3\text{MLCT} \rightarrow ^3\text{T}$ in 150 fs and $^3\text{T} \rightarrow ^5\text{T}$ in 70 fs.¹³ From a theoretical perspective, one of us performed several studies based on Fermi's golden rule. The deactivation path via the ^3MC states was confirmed in the symmetric structures,¹⁴ but the presence of geometrical distortions reopened the direct transfer from the $^1,^3\text{MLCT}$ band, becoming both paths competitive.¹⁵ Recently, Pápai published a study about the LIESST in $[\text{Fe}(\text{NCH})_6]^{2+}$, where only MC states play a role, based on quantum dynamic simulations.¹⁶ He constructed a vibronic Hamiltonian along the three main modes (Fe-N stretchings) and determined an ultrafast first ISC $^1\text{T}_{1g} \rightarrow ^3\text{T}_{2g}$ in 100 fs and a second slower ISC to the ^5T .

Despite the important amount of LIESST studies, of which only a few are mentioned in the above paragraph, the number of studies on the reverse process is scarce. Marino et al. studied the reverse-LIESST after the excitation to the $^5\text{E}_g$ in $[\text{Zn}_{1-x}\text{Fe}_x(\text{ptz})_6](\text{BF}_4)_2$, where ptz=1-propyltetrazole, using ultrafast pump-probe spectroscopy.¹⁷ Following the time-resolved excited-state absorption (ESA), they established that two different transitions are involved in the process, whose rates were determined by a double exponential fitting. The first one was attributed to the $^5\text{E}_g \rightarrow ^3\text{T}_{1g}$ in 1.7 ps ISC and the second to the $^3\text{T}_{1g} \rightarrow ^1\text{A}_{1g}$ in 39 ps. The quantum yield was determined to be 0.1 for the reverse-LIESST and 0.8 for the LIESST in $[\text{Fe}(\text{ptz})_6](\text{BF}_4)_2$ at 10K, with a branching ratio $^3\text{T}_1 \rightarrow ^5\text{T}_2 / ^3\text{T}_1 \rightarrow ^1\text{A}_1$ of 4:1.¹⁸

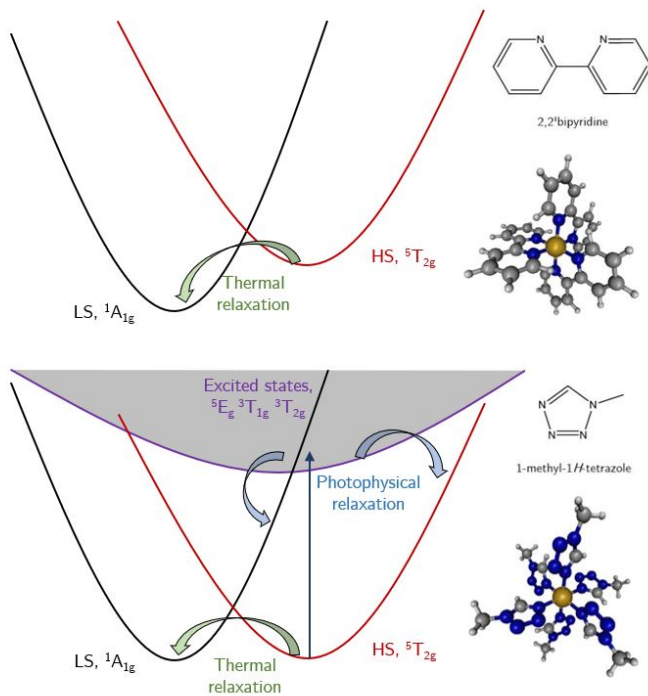


Fig. 1 Schematic diagram of the main electronic states involved in thermal HS→LS transition in $[\text{Fe}(\text{bpy})_3]^{2+}$ (top) and in the thermal and photoinduced relaxation in $[\text{Fe}(\text{mtz})_6]^{2+}$ (bottom).

In the current study, we simulated the thermal and light-induced conversion from the high-spin to low-spin in $[\text{Fe}(\text{bpy})_3]^{2+}$, where bpy=2,2'-bipyridine and $[\text{Fe}(\text{mtz})_6]^{2+}$, mtz = 1-methyl-1H-tetrazole. Two different processes have been studied, the HS→LS thermal relaxation and the photophysical process upon the absorption of a photon from the HS ($^5\text{T}_{2g} \rightarrow \text{E}_g$), i.e. the reverse-LIESST. The study of the thermal process is based on Fermi's golden rule and the photo process has been performed using wave-packet quantum dynamics with a vibronic model Hamiltonian.

Thermal relaxation. The HS→LS direct transfer has been studied in two Fe(II) complexes with significantly different HS-LS relative energies. $[\text{Fe}(\text{bpy})_3]^{2+}$ is a commonly studied complex with short-living HS state and $[\text{Fe}(\text{mtz})_6]^{2+}$ is either a paramagnetic or diamagnetic complex depending on the temperature. The intersystem crossing rate has been calculated using the Fermi's golden rule within the Condon approximation, which allows to express the rate as a direct product between the vibrational overlap and the (effective) spin-orbit coupling.

$$k_{ISC}^{a \rightarrow b} = \frac{2\pi}{\Omega_a} \sum_{\alpha} \sum_{\gamma} |\langle \psi_a^{\alpha} | \hat{H}_{SO} | \psi_b^{\gamma} \rangle|^2 \sum_{j=0,k} |\langle \{v_{aj}\} | \{v_{bk}\} \rangle|^2 \delta(E_{aj} - E_{bk}) \quad (1)$$

Herein ψ_a^{α} and ψ_b^{γ} are the spin-free electronic wave functions where a and b label electronic states of different multiplicity and α and γ are, respectively, the MS-components of the initial and final states. j and k are the vibronic levels, E_{aj} and E_{bk} are, respectively, the energies of the electronic state a in vibrational level j and electronic state b in vibrational level k , $E_{bk} = E_b + (k+1)\hbar\omega_k/2$. Ω_a is the degeneracy of the initial state and $\langle \{v_{aj}\} | \{v_{bk}\} \rangle$ is the two-center Franck-Condon integral. Note that this is the vibrationally cold approximation and the vibrational level of the initial state is fixed, $j=0$.

The effect of temperature is taken into account by the introduction of the Boltzmann distribution in the initial vibronic states.

$$k_{ISC}^{a \rightarrow b} = \frac{2\pi}{Z\Omega_a} \sum_{\alpha} \sum_{\gamma} |\langle \psi_a^{\alpha} | \hat{H}_{SO} | \psi_b^{\gamma} \rangle|^2 \times \sum_{j,k} e^{-\beta E_j} |\langle \{v_{aj}\} | \{v_{bk}\} \rangle|^2 \delta(E_{aj} - E_{bk}) \quad (2)$$

where $Z = \sum_j e^{-\beta E_j}$ is the canonical partition function for vibrational term in the initial state, E_j is the vibrational energy of the level j and β is $1/(k_B T)$, in which k_B is the Boltzmann constant.

We have mainly used the time-dependent approach, obtained after Fourier transform the δ function in Eq. 1, implemented in the VIBES program.¹⁹ Then, the rate is determined analytically and the number of grid points and the spacing between them to perform the discrete Fourier transform were selected upon convergence of the correlation and cumulant functions. In one case, we have used the time-independent approach for comparison. η , the threshold that determines the number of vibronic states included, was chosen as 1000 cm^{-1} after some testing of its influence. The basic ingredients for these calculations of the rates are:

i) the vibrational normal modes and frequencies of the states to account the vibrational overlap; ii) the adiabatic electronic energy difference between the states, and iii) the modulus of (effective) spin-orbit among the different spin components of each state.

The vibrational modes and frequencies are computed after a geometry optimization for the lowest singlet (LS) and quintet (HS) states using the TurboMole package.²⁰ The Perdew-Becke-Ernzerhof (PBE0) hybrid functional is used in combination with the triple- ζ valence polarized Gaussian-type basis set, def2-TZVP. Two-electron integrals are approximated by the resolution of identity (RI) using the auxiliary basis def2-universal-JFIT. The hessian matrix is calculated through analytical second derivatives and no symmetry restrictions are imposed during the optimization procedure.

The B3LYP adiabatic energies are unfortunately not accurate enough in Fe(II) complexes to be used for further analysis. Therefore, we determine the adiabatic energies with CASPT2 and shift the DFT potentials accordingly. Unfortunately, the DFT minimum considerably differs from the CASPT2 one and we carry out a relaxed scan along the main reaction coordinate, the Fe-N symmetric stretching. The geometries at each point are optimised through a constrained optimization at B3LYP/def2-SVP level. C_2 symmetry is imposed in the case of $[\text{Fe}(\text{bpy})_3]^{2+}$ and no symmetry restrictions are applied in $[\text{Fe}(\text{mtz})_6]^{2+}$. The Fe-N distances for the LS and HS states in the relaxed scan minima are in good agreement with the (XMS-)CASPT2 fully optimized geometries by Finney et al.²¹ Further information about the relaxed scan is found in SI.

CASPT2 calculations are performed using (Open)Molcas.²² The basis sets used are ano-rcc type with the following contractions: (7s6p5d4f3g2h) for the Fe, (4s3p1d) for N bonded with Fe, (3s2p) for C and the other N and (2s) for H atoms. Cholesky decomposition for the two-electron integrals is used to speed up the calculations. The reference wave function is a CASSCF state-averaged (SA) wave function, including the four lowest states for the singlets, the six lowest for the triplets and the five lowest for the quintets. The active space is formed by 10 electrons distributed over 12 orbitals, three more orbitals are added to those calculations that include MLCT states. The molecular orbitals for these systems are well-established^{23,24} and include two σ orbitals mainly corresponding to a small bonding interaction between ligands and Fe, the three 3d (t_{2g}) orbitals of Fe, the two 3d (e_g) orbitals of Fe with a small anti-bonding contribution respect to the ligands, an additional set of five 4d orbitals on Fe to introduce radial electron correlation²⁵. The influence of the MLCT states has also been studied expanding the active space by including three π^* orbitals corresponding to the aromatic system of the ligands. The perturbational treatment is carried out in all the electrons except the deep core ones Fe (1s2s2p), C and N (1s) and an imaginary shift of $0.15 E_h$ is used.

The spin-orbit coupling is calculated using Molcas²² in the singlet-quintet minimum energy crossing point geometry and in several conformations of the metadynamics for the LS and HS in $[\text{Fe}(\text{bpy})_3]^{2+}$. The settings for CASPT2 calculations are the same as for the adiabatic energy differences. The direct coupling is determined using the effective one-electron Douglas-Kroll-Hess (DKH)

Hamiltonian. The off-diagonal spin-orbit matrix elements are calculated by state interaction²⁶ using the CASSCF wave functions and the diagonal matrix elements are replaced by the CASPT2 energies. The direct coupling between states with $\Delta S=2$, such as singlet and quintet states, is strictly zero using the standard effective one-electron spin-orbit operators such as the DKH Hamiltonian. However, these states may have a non-vanishing effective coupling through intermediate states, which are states with non-zero direct coupling simultaneously with both states. In this case, triplet states can couple singlet and quintet states simultaneously. The effective Hamiltonian is constructed using the orthonormalised projections of SO wave functions $\tilde{\Psi}_k^\perp$ and their respective eigenvalues E_k using Bloch's formula.

$$H_{ij}^{SO,eff} = \langle \psi_i | \hat{H}^{SO,eff} | \psi_j \rangle = \langle \psi_i | \left[\sum_{k \in S_0} |\tilde{\Psi}_k^\perp\rangle E_k \langle \tilde{\Psi}_k^\perp| \right] | \psi_j \rangle \quad (3)$$

Herein, $\tilde{\Psi}_k^\perp$ is the des Cloizeaux orthonormalised spin-orbit wave function expressed in the basis of the spin-free states $\{\psi\}$ spanning a smaller subspace S_0 and E_k are the spin-orbit energies.

The effective Hamiltonian theory is an accurate and elegant way to determine effective couplings but it is difficult to extract information about the intermediate states that allow the coupling. For this reason, the weight of the intermediate triplet states in the singlet-quintet coupling was studied using second order Quasi-Degenerate Perturbation Theory (QDPT2) in different conformations. QDPT2 allows to decompose the spin-orbit coupling as a sum over the different intermediate states.

$$H_{ij}^{SO,QDPT2} = \langle \psi_i | \hat{H}^{SO} | \psi_j \rangle + \sum_{\mu \neq i,j} \frac{\langle \psi_i | \hat{H}^{SO} | \psi_\mu \rangle \langle \psi_\mu | \hat{H}^{SO} | \psi_j \rangle}{E_\mu - E_j} \quad (4)$$

Here, $\{\psi\}$ are the spin-free states and $\{E\}$ the spin-free energies. ψ_i and ψ_j are, respectively, the singlet and quintet states and ψ_μ the intermediate states.

The results in Table 1 show that ${}^3T_{1g}$, the lowest set of 3MC states, have the largest influence in the coupling of the singlet and quintet states. This can be easily rationalised because it is the intermediate state closest in energy to the singlet and quintet and has a strong direct coupling with both states. In addition, the decomposition also showed an almost negligible influence of the 3MLCT states in the coupling of the ${}^1A_{1g}$ and ${}^5T_{2g}$ states.

Table 1 also show discrepancies between the effective Hamiltonian theory and the quasi-degenerate perturbation theory. These differences are mainly associated to two intrinsic characteristics of the perturbative method used. The first is that QDPT2 loses accuracy when the initial and final states have larger energy differences. Eq. 4 shows that the larger the difference between E_i and E_j , the larger the difference becomes between H_{ij} and H_{ji} . The relative similarity of the couplings with both methods in the ISC geometry where singlet and quintet are quasi degenerate in comparison with the disagreement in most of the conformations where the energy difference is larger helps to corroborate this observation. The other shortcoming is that in QDPT2 the interactions are expanded up to second order and only the interactions through one intermediate state are accounted for, while all higher order terms are taken into account in the effective Hamiltonian

Table 1 Influence of the intermediate states in the singlet-quintet spin-orbit coupling for $[\text{Fe}(\text{bpy})_3]^{2+}$. All the couplings and energies are expressed in cm^{-1} .

Conf.	Ψ_μ	$H_{S\mu}^{SO}$	$H_{\mu Q}^{SO}$	$\gamma_{S\mu Q}$	H_{QDPT}^{SO}	H_{eff}^{SO}	ΔE
ISC	$^3T_{1g}$	529	284	20.8	21.8	32.7	-186
	$^3T_{2g}$	55	232	1.0			
ISC*	$^3T_{1g}$	548	449	27.9	29.0	29.9	-317
	$^3T_{2g}$	56	248	1.0			
1a	$^3\text{MLCT}$	25	58	0.03	42.3	30.1	2615
	$^3T_{1g}$	526	252	40.3			
	$^3T_{2g}$	92	291	1.9			
2a	$^3T_{1g}$	516	464	32.2	34.4	28.2	696
	$^3T_{2g}$	123	275	2.2			
1b	$^3T_{1g}$	524	465	19.4	20.6	43.0	-5623
	$^3T_{2g}$	70	294	1.1			
2b	$^3T_{1g}$	519	452	23.8	25.4	37.0	-3168
	$^3T_{2g}$	99	273	1.6			

$$\Delta E = E(\text{HS}) - E(\text{LS}) \text{ in } \text{cm}^{-1}$$

ISC*: CAS(10,15); active space formed by 10 electrons distributed over 15 orbitals.

$\gamma_{S\mu Q}$ is the 2nd order perturbative correction from state μ .

$H_{S\mu}^{SO}$ and $H_{\mu Q}^{SO}$ are the average matrix elements $\langle \Psi_S | \hat{H}^{SO} | \Psi_\mu \rangle$ and $\langle \Psi_\mu | \hat{H}^{SO} | \Psi_Q \rangle$, respectively.

The labels a and b refers to conformations from the singlet and quintet metadynamics simulations, respectively.

theory.

The influence of the thermal disorder in the spin-orbit coupling, and therefore, in the intersystem-crossing rates was also studied. Previously, it was demonstrated by one of us that the geometrical distortions have a strong effect on the size of the coupling, especially when MLCT states are involved. These changes in the couplings changed the rates of some of the intersystem-crossings by a few orders of magnitude in Fe(II) polypyridinal complexes.¹⁵ However, in the case of the ^1MC - ^5MC coupling, the effect of geometrical distortions is almost negligible, giving in all the conformations the same order of magnitude for the couplings and, therefore, the rates (or lifetimes).

Table 2 Singlet quintet effective spin-orbit coupling in cm^{-1} at different conformations and its corresponding lifetime using different approaches in $[\text{Fe}(\text{bpy})_3]^{2+}$.

Sys.	Conf.	$H^{SO,eff}$	T = 0K τ /ns	T=300K τ /ns	T=0K τ_{FC}
bpy	ISC	32.7	77.9	2.14	-
	ISC(10,15)	29.9	92.8	2.54	-
	1a	30.1	91.7	2.51	-
	2a	28.2	104.7	2.87	-
	Avg. ^(a)	28.1	106.1	2.9	-
	1b	43.0	45.0	1.24	-
	2b	37.0	60.7	1.66	-
	Avg. ^(b)	37.5	61.1	1.67	-
mtz	ISC	31.4	8.9 s	-	~ 10 years

^(a) Average of the ten structures extracted from the singlet metadynamics.

^(b) Average of the ten structures extracted from the quintet metadynamics.

The labels a and b refers to conformations from the singlet and quintet simulations, respectively.

The results show that the spin-orbit coupling strength is almost

identical for both complexes. However, the HS-LS vibrational overlap is completely different in the two complexes, what is the responsible for the different HS lifetimes in these complexes. Temperature is also important an important factor; the rates at 300 K are one order of magnitude faster than those at 0K using the vibrationally cold approximation. The HS state lifetime in $[\text{Fe}(\text{bpy})_3]^{2+}$ computed with the methodology described here is in good agreement with the 700 ps determined by Consani et al. for the same complex in aqueous solution²⁷, while the very slow ISC rate for $[\text{Fe}(\text{mtz})_6]^{2+}$ is indicative of a stable HS spin, as observed in experiment. Fermi's golden rule methodology is presented as an appropriate method to determine the order of magnitude of the HS state lifetime in Fe(II) complexes.

Photophysical relaxation. The reverse-LIESST is studied from the 5E_g state, after an excitation from the high spin state ($^5T_{2g} \rightarrow ^5E_g$). The process is studied in $[\text{Fe}(\text{mtz})_6]^{2+}$ because of the large HS state lifetime in this complex and the presence of experimental studies in an analogue complex, $[\text{Fe}(\text{ptz})_6]^{2+}$.¹⁷ In the high-spin minimum geometry, the $^5\text{MLCT}$ states are clearly higher in energy than the ^5MC states, therefore the former are highly unlikely to play a role in the deactivation and only the latter are included in the study. The reverse-LIESST was in a first attempt studied using Fermi's golden rule, as a follow-up of the satisfactory results reported in the literature for the singlet-quintet conversion. The only energetically favourable intersystem crossing transition from the 5E_g state to the triplets is the $^5E_g \rightarrow ^3T_{1g}$. However, the rate for this transition using the Fermi's golden rule is about a few milliseconds, several orders of magnitudes slower than the experimental reported value of 1.7 ps. For this reason, the process is studied using wave-packet quantum dynamic simulations with a vibronic model Hamiltonian.

The simulations are carried out with the Multi-Configuration Time-Dependent Hartree (MCTDH) method (Heidelberg package, version 8.5.13).²⁸ The basis of the method is to solve the time-dependent Schrödinger equation using the following *ansatz* for the nuclear wave function:

$$\Psi(q_1, q_2, \dots, q_p, t) = \sum_{j_1=1}^{n_1} \dots \sum_{j_p=1}^{n_p} A_{j_1 \dots j_p}(t) \prod_k \phi_{j_k}^{(k)}(q_k, t) \quad (5)$$

Herein, A_j are the expansion coefficients and ϕ_j are the single-particle functions (SPFs), which are linear combinations of primitive functions. In this case, the primitive functions take the shape of the n_j 's lowest solutions for an harmonic oscillator. The multi-set formalism is employed, where a different wave function is written for each state

$$\Psi^m(q_1, q_2, \dots, q_p, t) = \sum_{\alpha=1}^{\sigma} \Psi^{(\alpha)}|\alpha\rangle \quad (6)$$

where σ is the number of electronic states. We have included 5 SPFs for each state along each mode and 151 primitive functions for each mode.

The vibronic-coupling model Hamiltonian takes the following

shape:

$$\hat{H}(\{q\}) = \sum_{S=0}^2 \sum_{n=1}^{N_S} \sum_{\alpha=-|S|}^{|S|} \left[\left(T_N(\{q\}) + V_n^S(\{q\}) \right) |n_{S,\alpha}\rangle \langle n_{S,\alpha}| \right. \\ \left. + \sum_{n' \neq n}^{N_S} W_{n,n',S}^{NA}(\{q\}) |n_{S,\alpha}\rangle \langle n'_{S,\alpha}| \right] \\ + \sum_{S=0}^2 \sum_{n=1}^{N_S} \sum_{\alpha=-|S|}^{|S|} \sum_{S'=1}^2 \sum_{n'=1}^{N_{S'}} \sum_{\alpha'=-|S'|}^{|S'|} \left[W_{nS\alpha,n'S'\alpha'}^{SO} |n_{S,\alpha}\rangle \langle n'_{S',\alpha'}| \right. \\ \left. + W_{n'S'\alpha',nS\alpha}^{SO,*} |n'_{S',\alpha'}\rangle \langle n_{S,\alpha}| \right] \quad (7)$$

Herein, S is the spin quantum number, N_S is the number of states with S spin quantum number and α is the M_S component. $T_N(\{q\})$ is the nuclear kinetic energy, $V_n^S(\{q\})$ is the diabatic potential, $W_{n,n',S}^{NA}(\{q\})$ is the non-adiabatic coupling and $W_{nS\alpha,n'S'\alpha'}^{SO}$ and its hermitian conjugate $W_{n'S'\alpha',nS\alpha}^{SO,*}$ are the spin-orbit coupling terms. Note that in our model spin-orbit is coordinate independent while the other terms are coordinate dependent.

The nuclear kinetic energy is defined (in atomic units) as

$$T_N = - \sum_i^{N_{vib}} \frac{\omega_i}{2} \frac{\partial^2}{\partial q_i^2} \quad (8)$$

where ω_i is the frequency of the HS state in mode i and N_{vib} is the number of vibrations included in the model Hamiltonian.

The diabatic potential is defined using a quartic polynomial expression

$$V_n^S = E_n^S + \sum_i^{N_{vib}} \sum_{j=1}^4 \frac{1}{j!} k_{j,i}^{n,S} q_i^j \quad (9)$$

Here E_n^S is the diabatic energy for the state n with spin S at the Franck-Condon region and $k_{j,i}^{n,S}$ is the j^{th} expansion term along vibrational mode i for this state.

The non-adiabatic coupling term is described as

$$W_{n,n',S}^{NA} = \sum_i^{N_{vib}} \lambda_i^{n,n',S} q_i \quad (10)$$

where $\lambda_i^{n,n',S}$ is a linear-expansion coefficient for the non-adiabatic coupling between states n and n' with spin S along mode i .

The spin-orbit coupling term is defined as follows

$$W_{nS\alpha,n'S'\alpha'}^{SO} = \langle n_{S\alpha} | \hat{H}^{SO} | n'_{S'\alpha'} \rangle \quad (11)$$

where \hat{H}^{SO} is the DKH Hamiltonian, $\langle n_{S\alpha} |$ is the state n with spin S and $M_S \alpha$ and $|n_{S'\alpha'}\rangle$ is the state n' with spin S' and $M_{S'} \alpha'$.

The model is constructed by the expansion along the most representative modes of the HS state optimized at PBE0/def2-TZVP level and includes the electronic states $^1A_{1g}$, $^1T_{1g}$, $^3T_{1g}$, $^3T_{2g}$, $^5T_{2g}$ and 5E_g , which generates a model of 47 states taking into account the spatial and spin symmetries. The terms for the Hamiltonian are obtained through a fitting procedure of the XMS-CASPT2 energies. These calculations are carried out using an active space of 10 electrons distributed over 12 molecular orbitals. The per-

turbative treatment of the electron correlation is applied to all electrons except the deep core ones Fe (1s2s2p) and C, N (1s) and the 30 highest orbitals. An imaginary level shift of 0.25 E_h is applied to avoid intruder state problems. From the adiabatic energies along the main modes, we obtain the diabatic energies as a quartic polynomial and the non-adiabatic couplings between states of the same M_S value within the linear-expansion approximation. The off-diagonal terms between states of different M_S are included with the spin-orbit coupling at the DFT optimised geometry. The nuclear kinetic energy operators in mass-frequency-weighted coordinates are added using the frequencies of the HS state at DFT level. The simulations are initialised after a relaxation of the wave-packet in the $^5T_{2g}$ state, which starts the dynamics at the minimum energy geometry of the HS state and the wave-packet is distributed over the different components of the 5E_g state according to the oscillator strengths. Further (numerical) information about the couplings is given in the SI.

The selected normal modes are chosen based on those modes with the largest reorganization energy connecting the minima of the different states involved in the process. The difference between the optimized geometries for each state at DFT level is projected into the HS state normal modes, following the expression

$$q_k^A = \omega_k^{1/2} \sum_l L_{kl}^{HS} m_l^{1/2} (\mathbf{R}_{A,l} - \mathbf{R}_{HS,l}) \quad (12)$$

Herein, q^A is the normal mass-frequency-weighted Cartesian coordinate expanding the geometrical differences between state A and the HS state projected in the basis of HS state reference normal modes. m_l the mass of atom l , \mathbf{R}_A and \mathbf{R}_{HS} are the Cartesian geometries for states A and the HS state, respectively and L^{HS} is the matrix that contains the eigenvectors of the HS state normal modes.

Table 3 Coordinates q^A of the main electronic states involved in reversed LIESST projected on the HS state normal modes. In parenthesis the value of q^A , those modes with values larger than 1 are reported here. The modes in the reaction coordinate are in bold.

	Included modes	Excluded modes
$^1A_{1g}$ - $^5T_{2g}$	42 (-8.95), 30 (-1.99) 10 (1.72), 39 (1.63)	-
$^3T_{1g}$ - $^5T_{2g}$	42 (-4.28), 31 (2.50), 33 (2.34)	29 (-2.05), 165 (1.79) 11 (-1.11)
5E_g - $^5T_{2g}$	42 (3.89), 31 (-3.42) 33 (-1.36), 10 (-1.28)	29 (2.97), 11 (2.00) 21 (1.31), 28 (-1.17)

According to this analysis, there are three main modes representing the reverse-LIESST. These modes have Fe-N stretching character, q_{42} is the symmetric motion and q_{31} and q_{33} correspond to Fe-N asymmetric stretching vibrations, which are specially important for Jahn-Teller active states. This model with three Fe-N modes coincides with the one proposed by Papai in his study of the LIESST for $[\text{Fe}(\text{NHC})_6]^{2+}$. In our model, we include the two asymmetric modes q_{31} , q_{33} and the reaction coordinate mode (q_{rc}) that connects HS and LS geometries which is a com-

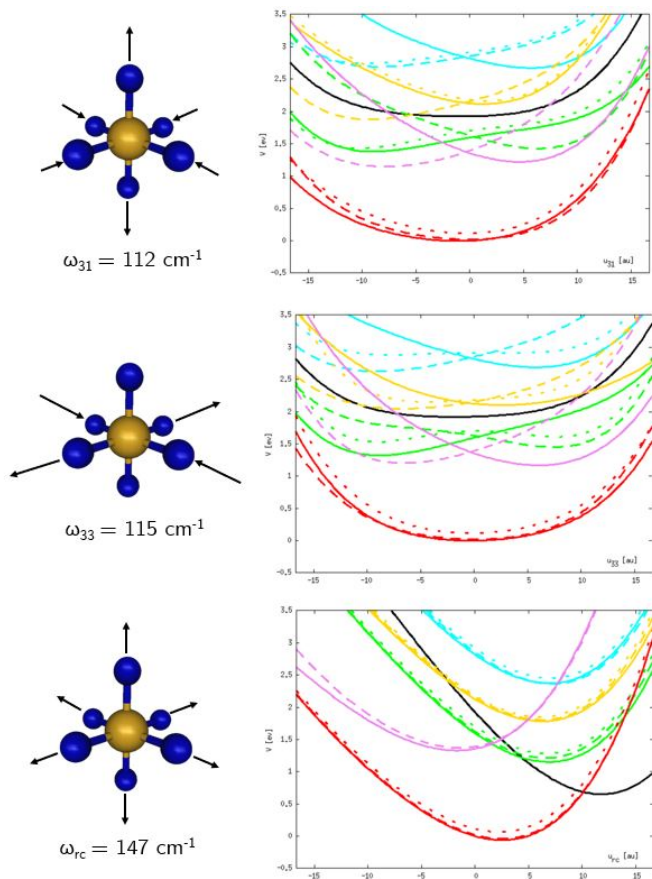


Fig. 2 Schematic motions and diabatic potentials along the modes q_{31} , q_{33} and q_{rc} . ${}^1A_{1g}$ in black, ${}^1T_{1g}$ in cyan, ${}^3T_{1g}$ in green, ${}^3T_{2g}$ in gold, ${}^5T_{2g}$ in red and 5E_g in violet. The different components are represented with solid, dashed and dotted lines.

binned mode described as:

$$q_{rc} = 0.95q_{42} + 0.21q_{30} - 0.18q_{10} - 0.17q_{39} \quad (13)$$

This reaction coordinate mode describes the Fe-N symmetric breathing (q_{rc}) but slightly assisted for N-Fe-N bending modes (q_{30} , q_{10} , q_{39}) which aids to adapt the N-Fe-N angles to each Fe-N distance.

The reaction coordinate mode does not break the pseudo- O_h symmetry. In this mode, the triple degeneracy of ${}^1T_{1g}$, ${}^3T_{1g}$, ${}^3T_{2g}$, ${}^5T_{2g}$ and the double degeneracy of 5E_g is maintained. The Fe-N asymmetric stretching (q_{31}) is described as a compression of the four Fe-N distance for the N in the equatorial plane with an elongation of the two Fe-N distances for the axial N. This breaks the pseudo- O_h symmetry to a pseudo- D_{4h} , which breaks the triple degenerate states into doubly degenerate states and remove the degeneracy for the 5E_g states. In the other asymmetric stretching (q_{33}), the axial N remain in place while the two equatorial N come closer and recede in pairs. After this motion, the pseudo- O_h symmetry is broken to a pseudo- D_{2h} that removes the degeneracy for all the states.

The efficiency of an intersystem-crossing depends on the energy difference between a pair of states and the size of their coupling. In this complex, the energetically accessible intersystem-

crossing from the 5E_g is the ${}^5E_g \rightarrow {}^3T_{1g}$. Near the absorption geometry, that is the ${}^5T_{2g}$ minimum, ${}^3T_{1g}$ is slightly lower in energy than 5E_g , therefore, a crossing between these states is found after the absorption. However, the gradients to the 5E_g minimum are high and the system will evolve to this region where the energy gap between the quintet and the triplet is large and the efficiency of the ISC small. The transition to the ${}^3T_{2g}$ is discarded because these states are above the 5E_g states in the absorption region.

Despite the energy gap does not seem to favour the ISC transfer, this could still be efficient when there exists a large coupling between the states. This is not the case for the 5E_g - ${}^3T_{1g}$ coupling, which is about 10 cm^{-1} in average at the ${}^5T_{2g}$ DFT minimum. The small coupling can be easily rationalized observing the two electrons of difference in the main configurations of the ${}^5E_g(t_{2g}^3 e_g^2)$ and ${}^3T_{1g}(t_{2g}^5 e_g^1)$, which are strictly uncoupled in the usual effective one-electron spin-orbit operator.

The minimum of the 5E_g is energetically far away from the other states, 5E_g is lower in energy than ${}^3T_{1g}$ and above the ${}^5T_{2g}$, well separated from both. Despite the large energy gap with these other states, the nuclear kinetic energy may bring the wavepacket to regions with nearly degenerate ${}^5T_{2g}$ - 5E_g , in a sloped conical intersection. Unfortunately, this intersection could not be determined because of the lack of an accurate computational method to determine precisely at the same time geometries (for the minima of states and minimum energy crossings) and energies at an affordable computational cost. The plausibility of the crossing in the quintets is also not favoured by the energy difference between the states in the regions around the 5E_g minimum but at least there is a strong coupling with values larger than 250 cm^{-1} . This coupling is strong, as expected for the one-electron of difference between the states in their dominant configurations ($t_{2g}^4 e_g^2$ and $t_{2g}^3 e_g^3$). These ingredients induce to think that the most favourable transition is the ${}^5E_g \rightarrow {}^5T_{2g}$.

The evolution of the diabatic population (Fig. 3) shows that almost half of the population of the 5E_g is rapidly transferred to the ${}^5T_{2g}$ state. Then, part of the remaining population in the 5E_g evolves to the ${}^5T_{2g}$ when the wave-packet visits regions with small energy gap between both states. From, this state part of the population is gradually transferred to the ${}^3T_{1g}$, above 10% in 2 ps, from which the LS may be populated. This last event is not appreciated in our dynamics because it happens in a larger time scale than our simulation time.

Our results indicates a faster ${}^5E_g \rightarrow {}^5T_{2g}$ transition than experimentally observed. This unexpectedly fast rate is probably because of the limitation of the model Hamiltonian. The complete vibrational space is not represented but it is reduced to the three main coordinates. Moreover, the diabatic coupling terms between modes are not included in the model. These terms may be especially important in the description of Jahn-Teller modes. The lack of this terms gives stronger gradients in the model and the wavepacket may visit rapidly regions with small ${}^5T_{2g}$ - 5E_g energy gaps with high efficient population transfer. Unfortunately, the inclusion of these terms dramatically increase the computational cost of these calculations. In addition, the spin-orbit coupling is fixed at the HS geometry and the variation along coordinates, vibronic

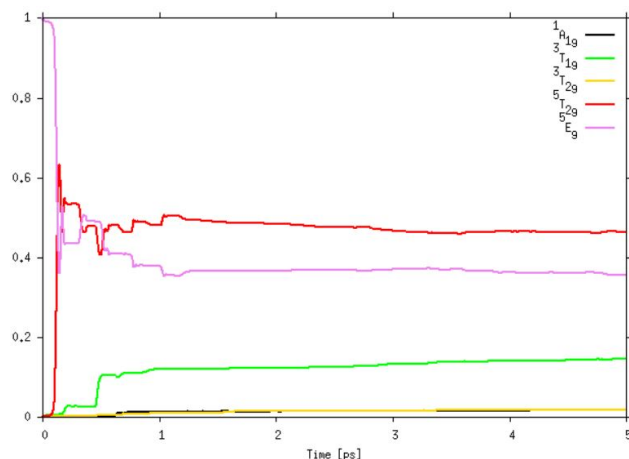


Fig. 3 Time-evolution population of the diabatic states along the dynamics. The states are represented by the colours: $^1A_{1g}$ black, $^1T_{1g}$ cyan, $^3T_{1g}$ green, $^5T_{1g}$ red and 5E_g violet.

spin-orbit coupling, is not included in our model.

The quintet-quintet transition observed in the wave-packet quantum dynamics is also determined by Fermi's golden rule. The calculated lifetime for the 5E_g at OK is 2.3 ps, in good agreement with the first transition determined by Marino et al. in $\text{Fe}(\text{ptz})_6$.¹⁷ Then, calculations at different level of theory point in the same direction. The first transition into the reverse-LIESST process is the relaxation to the $^5T_{2g}$. After that, in a longer time scale, part of the population is transferred from the vibrationally hot HS state to the intermediate $^3T_{1g}$ and finally the $^1A_{1g}$.

To conclude, we have applied two different methodologies to study the thermal and photophysical conversions from the high-spin to the low-spin state. The order of magnitude of the HS state lifetime in the thermal relaxation process has been determined satisfactorily using Fermi's golden rule. The influence of the $^3T_{1g}$ as the main intermediate state coupling HS and LS has been demonstrated, while the role of the $^3\text{MLCT}$ states in this coupling can be neglected. This rate theory has been used to determine the HS state lifetime in $\text{Fe}(\text{II})$ complexes with nearly O_h symmetry. This may be also tested to determine the HS state lifetime in complexes breaking the symmetry such as $[\text{Fe}(\text{terpy})_2]^{2+}$, where the empirical energy gap rule is not valid.¹¹ The determination of the adiabatic energies is the key step in this process and would be done using an appropriate DFT functionals or with the recent algorithms to account for the (XMS-)CASPT2^{29,30} optimization implemented in quantum codes such as BAGEL.

The calculations indicate that the intersystem-crossing from the 5E_g to the triplets in the reverse-LIESST is not favourable. The mechanism that we propose according to the quantum dynamics is $^5E_g \rightarrow ^5T_{2g}^* \rightarrow ^3T_{1g} \rightarrow ^1A_{1g}$. The intersystem-crossing is produced from the vibrationally hot, $^5T_{2g}^*$ which is formally as a thermal relaxation at an effective high temperature. This path could explain the limitation on the results observed in Fermi's golden rule when it should work fine because it happens from the minimum of the excited state due to the rate of the transition. This also would explain the two different rates reported in the reverse-LIESST and the quantum yield reported by Marino et al.¹⁷ According to the

LIESST, the rate for the $^3T_{1g} \rightarrow ^5T_{2g}/^3T_{1g} \rightarrow ^1A_{1g}$ should be about 1.5 ps and the branching ratio 4:1. This does not compare with the 37 ps and the quantum yield of 0.1 associated to these transitions. For this reason and based on our results, we propose an alternative mechanism from the vibrationally hot $^5T_{2g}^*$ state. Our results do not match completely with the experimental reported rates, this may probably be associated with a limitation in our model Hamiltonian. New improvements in the generation model Hamiltonian such as the inclusion of diabatic coupling terms or vibronic spin-orbit may be explored.

Conflicts of interest

The authors declare no conflicts of interest.

Acknowledgements

MHR acknowledges financial support by the *Agence Nationale pour la Recherche* through the project MULTICROSS (ANR-19-CE29-0018). MAR and CdG acknowledge the Spanish ministry of Science and Innovation (Project PID2020-113187GB-I00). The project leading to this publication has received funding from the Excellence Initiative of Aix-Marseille Université - A*Midex, a French "Investissement d'Avenir" programme, AMX-21-ERC-01, and from the funding "ERC Booster" from Région Sud Provence-Alpes-Côte d'Azur.

Notes and references

- M. R. Geraskina, A. T. Buck and A. H. Winter, *J. Org. Chem.*, 2014, **79**, 7723–7727.
- W.-W. Wu, S.-G. Wu, Y.-C. Chen, G.-Z. Huang, B.-H. Lyu, Z.-P. Ni and M.-L. Tong, *Chem. Commun.*, 2020, **56**, 4551–4554.
- I. Krivokapic, M. Zerara, M. L. Daku, A. Vargas, C. Enachescu, C. Ambrus, P. Tregenna-Piggott, N. Amstutz, E. Krausz and A. Hauser, *Coord. Chem. Rev.*, 2007, **251**, 364–378.
- G. G. Morgan, K. D. Murnaghan, H. Muller-Bunz, V. McKee and C. J. Harding, *Angew. Chem. Int. Ed.*, 2006, **45**, 7192–7195.
- D. J. Harding, P. Harding and W. Phonsri, *Coord. Chem. Rev.*, 2016, **313**, 38–61.
- O. I. Kucheriv, I. O. Fritsky and I. A. Gural'skiy, *Inorganic Chim. Acta*, 2021, **521**, 120303.
- A. Gaspar, M. Seredyuk and P. Gütllich, *J. Mol. Struct.*, 2009, **924-926**, 9–19.
- A. Arroyave, A. Lennartson, A. Dragulescu-Andrasi, K. S. Pedersen, S. Piligkos, S. A. Stojan, S. M. Greer, C. Pak, O. Hietsoi, H. Phan, S. Hill, C. J. McKenzie and M. Shatruk, *Inorg. Chem.*, 2016, **55**, 5904–5913.
- S. Zerdane, M. Cammarata, O. Iasco, M.-L. Boillot and E. Collet, *J. Chem. Phys.*, 2019, **151**, 171101.
- G. Molnár, L. Salmon, W. Nicolazzi, F. Terki and A. Bousseksou, *J. Mater. Chem. C*, 2014, **2**, 1360.
- A. Hauser, C. Enachescu, M. L. Daku, A. Vargas and N. Amstutz, *Coord. Chem. Rev.*, 2006, **250**, 1642–1652.
- G. Auböck and M. Chergui, *Nat. Chem.*, 2015, **7**, 629–633.
- W. Zhang, R. Alonso-Mori, U. Bergmann, C. Bressler, M. Chollet, A. Galler, W. Gawelda, R. G. Hadt, R. W. Hartsock, T. Kroll, K. S. Kjaer, K. Kubiček, H. T. Lemke, H. W. Liang, D. A. Meyer, M. M. Nielsen, C. Purser, J. S. Robinson, E. I. Solomon, Z. Sun, D. Sokaras, T. B. van Driel, G. Vankó, T.-C. Weng, D. Zhu and K. J. Gaffney, *Nature*, 2014, **509**, 345–348.
- C. Sousa, C. de Graaf, A. Rudavskiy, R. Broer, J. Tatchen, M. Etinski and C. M. Marian, *Chem. Eur. J.*, 2013, **19**, 17541–17551.
- C. Sousa, M. Lluell, A. Domingo and C. de Graaf, *Phys. Chem. Chem. Phys.*, 2018, **20**, 2351–2355.
- M. Pápai, *Inorg. Chem.*, 2021, **60**, 13950–13954.
- A. Marino, P. Chakraborty, M. Servol, M. Lorenc, E. Collet and A. Hauser, *Angew. Chem. Int. Ed.*, 2014, **53**, 3863–3867.
- A. Hauser, in *Spin Crossover in Transition Metal Compounds II. Topics in Current Chemistry* by P. Gütllich and H. A. Goodwin, ed. P. Gütllich and H. A. Goodwin, Springer Berlin, Heidelberg, Germany, 2004, ch. Light-Induced Spin Crossover and the High-Spin \rightarrow Low-Spin Relaxation, pp. 155–198.
- M. Etinski, J. Tatchen and C. M. Marian, *J. Chem. Phys.*, 2011, **134**, 154105.
- TURBOMOLE V6.4.2 2012, a development of University of Karlsruhe and Forschungszentrum Karlsruhe GmbH, 1989-2007, TURBOMOLE GmbH, since 2007; available from <http://www.turbomole.com>.

- 21 B. A. Finney, S. R. Chowdhury, C. Kirkvold and B. Vlasisavljevich, *Phys. Chem. Chem. Phys.*, 2022, **24**, 1390–1398.
- 22 I. Fdez. Galván, M. Vacher, A. Alavi, C. Angeli, F. Aquilante, J. Autschbach, J. J. Bao, S. I. Bokarev, N. A. Bogdanov, R. K. Carlson, L. F. Chibotaru, J. Creutzberg, N. Dattani, M. G. Delcey, S. S. Dong, A. Dreuw, L. Freitag, L. M. Frutos, L. Gagliardi, F. Gendron, A. Giussani, L. González, G. Grell, M. Guo, C. E. Hoyer, M. Johansson, S. Keller, S. Knecht, G. Kovačević, E. Källman, G. Li Manni, M. Lundberg, Y. Ma, S. Mai, J. P. Malhado, P. A. Malmqvist, P. Marquetand, S. A. Mewes, J. Norell, M. Olivucci, M. Oppel, Q. M. Phung, K. Pierloot, F. Plasser, M. Reiher, A. M. Sand, I. Schapiro, P. Sharma, C. J. Stein, L. K. Sørensen, D. G. Truhlar, M. Ugandi, L. Ungur, A. Valentini, S. Vancoillie, V. Veryazov, O. Weser, T. A. Wesolowski, P.-O. Widmark, S. Wouters, A. Zech, J. P. Zobel and R. Lindh, *J. Chem. Theory Comput.*, 2019, **15**, 5925–5964.
- 23 K. Pierloot and S. Vancoillie, *J. Chem. Phys.*, 2006, **125**, 124303.
- 24 B. Ordejón, C. de Graaf and C. Sousa, *J. Am. Chem. Soc.*, 2008, **130**, 13961–13968.
- 25 K. Andersson and B. O. Roos, *Chem. Phys. Lett.*, 1992, **191**, 507 – 514.
- 26 B. O. Roos and P.-Å. Malmqvist, *Phys. Chem. Chem. Phys.*, 2004, **6**, 2919–2927.
- 27 C. Consani, M. Prémont-Schwarz, A. ElNahas, C. Bressler, F. van Mourik, A. Cannizzo and M. Chergui, *Angew. Chem.*, 2009, **121**, 7320–7323.
- 28 H. D. Meyer and O. Vendrell, <http://mctdh.uni-hd.de/>, 2013.
- 29 M. K. MacLeod and T. Shiozaki, *J. Chem. Phys.*, 2015, **142**, 051103.
- 30 B. Vlasisavljevich and T. Shiozak, *J. Chem. Theory Comput.*, 2016, **12**, 3781–3787.